Nano Research

Open Access

Research Article

MOF-derived ZnO nanocages with enhanced UV absorption and photocarrier dynamics for high-performance underwater photodetection and optical imaging

Xinghan Li[1,§], Zhitao Shao[1,§], Yuan Zhang[1], Dongyue Tian[1], Xinran Hu[1], Wenhui Li[1], Junxin Zhou[1], Nana Zhang[1], Sha Zhao[1], Jing Yao[2], Feng Gao[2] ✉, and Wei Feng[1] ✉

[1] *College of Chemistry, Chemical Engineering and Resource Utilization, Northeast Forestry University, Harbin 150040, China*
[2] *Key Laboratory for Photonic and Electronic Bandgap Materials, Ministry of Education, School of Physics and Electronic Engineering, Harbin Normal University, Harbin 150025, China*
§ *Xinghan Li and Zhitao Shao contributed equally to this work.*

Cite this article: *Nano Research*, **2025**, *18*, 94907403. https://doi.org/10.26599/NR.2025.94907403

ABSTRACT: Self-powered photoelectrochemical (PEC) photodetectors hold great promise for underwater optical applications, yet suffer from sluggish carrier dynamics and limited stability. Herein, high-performance, self-powered, and stable PEC ultraviolet (UV) photodetectors were fabricated using metal-organic-framework derived ZnO nanocages (NCs). These topography-engineered ZnO NCs synchronously enhance UV absorption, facilitate photogeneration carrier separation, and promote charge transfer at the ZnO/electrolyte interface, thus optimizing the overall photoresponse performance. The ZnO NCs-based PEC device achieves an ultrahigh responsivity of 300.6 mA/W under 365 nm UV light irradiation, a fast response time of 10/20 ms, outstanding spectra selectivity (UV/visible rejection ratio of 2000), and excellent cycling stability (10,000 cycles), which is one of the best reported PEC UV photodetectors. Furthermore, the self-powered ZnO-based PEC PDs have good underwater optical imaging capability. This work provides a new idea for designing high-performance UV photodetectors for application in underwater environments.

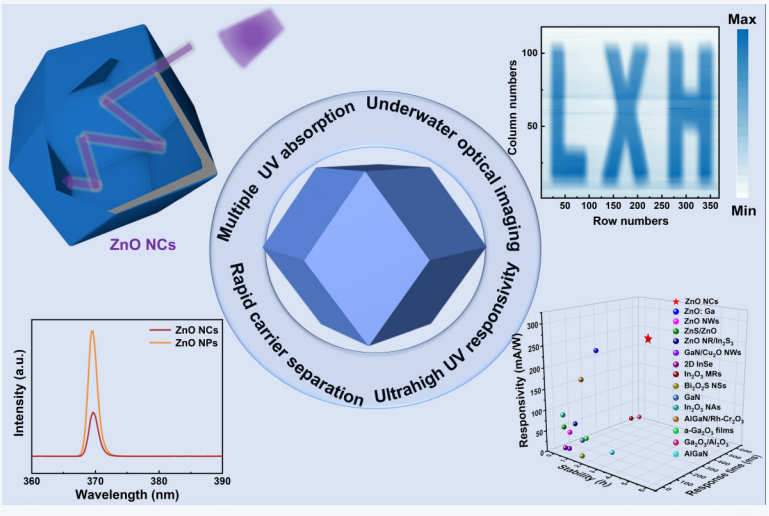

KEYWORDS: photoelectrochemical, ultraviolet (UV) photodetectors, self-powered, ZnO nanocages, underwater optical imaging

1 Introduction

In underwater applications, ultraviolet photodetectors (UV PDs) offer the advantages of low background noise and high selectivity in detecting substances compared to other wavelengths, such as visible and infrared light [1–5]. As emerging self-powered PDs, photoelectrochemical (PEC) UV PDs with high sensitivity and simple structure driven by the solid/liquid interfacial built-in electric field, have been investigated in several fields, including UV monitoring, medical testing, and underwater optical communication [6–9]. However, most photoelectrodes suffer from high photogenerated carrier recombination rates and sluggish interfacial electrochemical reaction kinetics, restricting their overall PEC UV detection performance [10]. p-n junctions and surface modification have been explored to enhance PEC UV photoresponse by facilitating photogenerated carrier separation and accelerating interfacial charge transfer [11, 12]. However, achieving

Received: March 6, 2025; **Revised:** March 25, 2025
Accepted: March 25, 2025

✉Address correspondence to Feng Gao, gaofeng@hrbnu.edu.cn; Wei Feng, wfeng@nefu.edu.cn

desirable UV photoresponse and reducing the complexity of fabrication processes remain significant challenges [13]. Therefore, the exploration of single active materials with suitable nanostructures that possess efficient UV photoelectric conversion and fast interfacial electrochemical kinetics remains a research focus on PEC UV PDs [14, 15].

Currently, various wide-bandgap nanomaterials with a strong UV photoresponse have been explored for designing PEC UV PDs [16, 17], such as TiO_2 [18], Ga_2O_3 [19], SnO_2 [20], and ZnO [21, 22]. Among them, a third-generation semiconductor material ZnO stands out, which is favorable for UV detection due to the wide bandgap of approximately 3.37 eV and good stability [23, 24]. Li et al. [25] used purified water as the electrolyte and fabricated a ZnO nanorod array as a PEC UV PD photoanode. The device achieved a maximum responsivity (R) of 22 mA/W within the wavelength range of 350–550 nm and a response time of less than 0.1 s. Lin et al. [26] developed a ZnO/ZnS core–shell nanorod array as the photoanode for a PEC UV PD. The ZnO/ZnS n-n junction and core–shell structure enhanced light absorption and improved photoresponse. The PD exhibits a fast response time of 0.04 s and a high R of 56 mA/W at 340 nm, which is 1.8 times higher than that of sole ZnO-based PD. Tang et al. [27] fabricated a Ga-doped ZnO PEC PD with an ultra-high R of 233.26 mA/W under 365 nm illumination and a fast response time of 159/150 ms without external bias voltage. However, the cycling stability is only maintained for 1 h (1800 cycles) with almost no attenuation of the photocurrent density (J_{ph}). Doping and heterojunction are powerful strategies for improving the performance of ZnO-based PEC PDs, but the corresponding fabrication processes are complicated. It is still a great challenge to achieve high-performance PEC photodetectors based on sole ZnO.

In this study, we successfully developed high-performance self-powered PEC UV PDs based on ZnO nanocages (NCs). The PDs exhibit an ultrahigh R of 300.6 mA/W under 365 nm irradiation and maintain nearly no decay photoresponse after 5.56 h of light exposure (10,000 cycles), demonstrating outstanding stability. The boosting photoresponse of ZnO PEC UV PDs can be ascribed to the NCs morphology, which not only enhances UV absorption but also promotes the separation of photogenerated carriers and accelerates ZnO/electrolyte interfacial electrochemical reaction kinetics. Furthermore, the devices show fast response speed and are successfully applied in the underwater optical imaging system demonstrating a proof-of-concept application. The high-performance ZnO NCs PEC UV PDs exhibit great promise in underwater UV detection and imaging, laying a solid foundation for practical application.

2 Experimental

2.1 Materials

2-Methylimidazole (2-$C_4H_6N_2$, 98%), methanol (99%), zinc nitrate hexahydrate ($Zn(NO_3)_2{\cdot}6H_2O$, 99%), potassium hydroxide (KOH, 99%), sulfuric acid (H_2SO_4, 99%), and fluorine-doped tin dioxide (FTO) glass were purchased from Shanghai McLean Biochemical Technology Co. All materials were used without additional purification.

2.2 Synthesis of ZnO NCs

First, the FTO substrate was ultrasonically treated with acetone, ethanol, and deionized water for 10 min, respectively. After washing, the FTO was immersed in concentrated H_2SO_4 (18.4 M) for 6 h and then was washed and blown dry. A 40 mL methanol solution containing $Zn(NO_3)_2{\cdot}6H_2O$ (0.594 g) and 2-$C_4H_6N_2$ (0.328 g) was stirred for 1 h. Next, the FTO substrate was placed flat in the mixed solution for 24 h. Finally, the Zn-ZIF-8 films (1 cm × 1 cm) were obtained by placing them in a 60 °C vacuum drying oven. The as-prepared Zn-ZIF-8 films were calcined in a muffle furnace at 400 °C in air for 3 h (heating rate: 5 °C/min).

ZnO nanoparticles (ZnO NPs): The ZIF-8 solution was collected and annealed in a 400 °C muffle for 3 h. 5 mg of ZnO NPs was weighed and dissolved in 1 mL of DMF by ultrasonication. A 200 μL drop of the sample mixture was taken on an FTO (1 cm × 1 cm) and dried in a vacuum oven at 60 °C overnight.

2.3 Materials characterization

The crystalline structure was analyzed via X-ray diffraction (XRD) at room temperature (Shimadzu XRD-6100 with Cu Kα radiation (λ = 1.5406 Å)). UV–visible (UV–vis) absorption spectra were recorded via a UV-3000 spectrophotometer. The morphology and microstructure were further investigated by scanning electron microscopy (SEM, JSM-7500F) and transmission electron microscopy (TEM, JEM-200 operated at 200 keV). Elemental composition was determined by X-ray photoelectron spectroscopy (XPS) performed with monochromatic Al Kα radiation (Thermo Scientific K-Alpha). Photoluminescence (PL) spectra were measured by a spectrometer (PerkinElmer LS 55) with an excitation laser at 250 nm.

2.4 Photoresponse measurements

The performance of the PEC PDs was evaluated in a three-electrode system which was achieved on an electrochemical workstation (CHI660E, CH Instruments) under a power-adjustable laser with wavelengths of 365 and 405 nm. The fabricated photoelectrodes, Pt sheet, and saturated calomel electrodes (SCE) were used as photoanode, counter electrode, and reference electrode, respectively. The electrolytes were 0.1 M KOH, 0.1 M Na_2SO_4, and simulated seawater. The PEC PDs were characterized using a polytetrafluoroethylene reaction cell with a transparent quartz optical window. For underwater light imaging, a hollow "LXH" logo made of steel plate was used as the test pattern and installed in front of the 365 nm laser. The imaging system was placed on a computer-controlled electric translation stage that can move continuously in the X and Y directions. The incident light first passed through the imaging object and then illuminated the surface of the detector. The electrical signals generated by the device were collected in real-time by the source meter (Keithley 6482) and oscilloscope. The computer recorded the position information of the translation stage while collecting signals from the detector, and ultimately obtained a pattern consistent with the imaging object.

3 Results and discussion

3.1 Characterization of ZnO NCs

The XRD pattern of ZIF-8 agreed with the simulated crystal model from the Ref. [28] (as shown in Fig. S1 in the Electronic Supplementary Material (ESM)), proving the successful preparation of ZIF-8 samples. As shown in Fig. S2 in the ESM, the ZIF-8 exhibits a dodecahedra structure with an average crystal size of

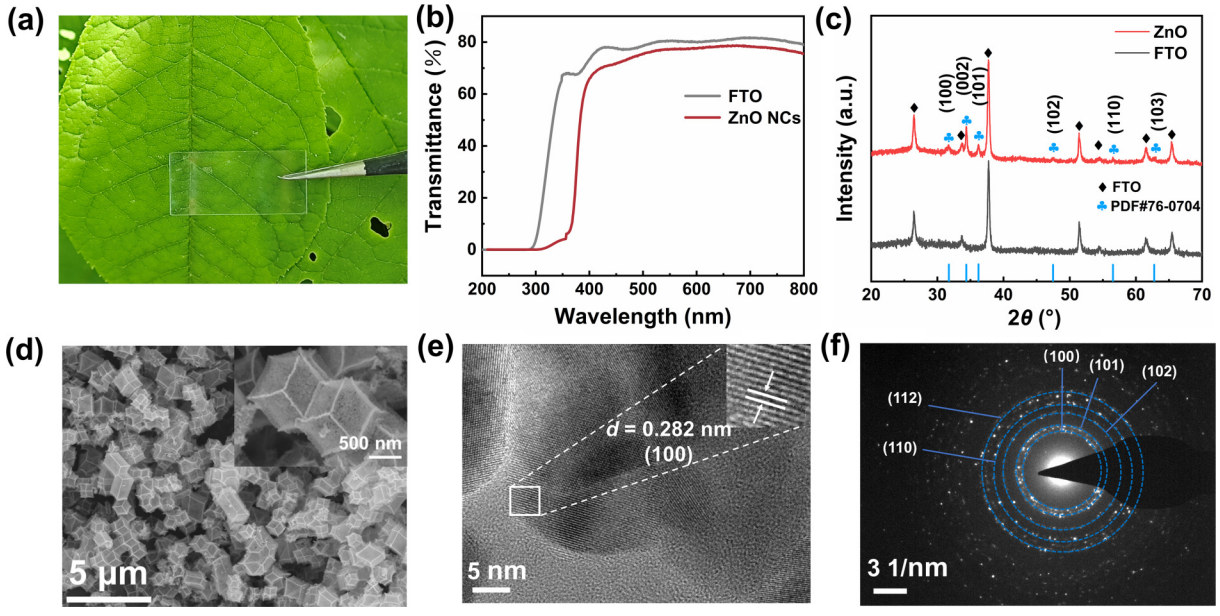

Figure 1 Characterization of the ZnO NCs. (a) Digital image of ZnO NCs photoanode. (b) Transmission spectra of ZnO NCs and FTO. (c) XRD patterns of ZnO NCs samples. (d) SEM image of ZnO NCs. Inset: SEM at high magnification. (e) HRTEM image of ZnO NCs. (f) SAED image of ZnO NCs.

approximately 800 nm. Figure 1(a) shows a digital image of ZnO NCs on FTO substrate with high transparency. The transmission spectra of the FTO substrate and ZnO NCs on FTO substrate are compared (Fig. 1(b)), and ZnO NCs on the FTO exhibit a transmittance of approximately 75% in the 400–800 nm range, which is close to the FTO substrate. Due to their high visible light transmittance and strong UV absorption, ZnO NCs are suitable for transparent UV optoelectronic devices and UV-blocking materials [29, 30]. Figure 1(c) shows the XRD pattern of ZnO NCs. Excluding the peak of the FTO substrate, the other peaks at 31.7°, 34.4°, 36.2°, 47.5°, 56.6°, 62.8°, 66.3°, 67.9°, 69.0°, and 72.5° match well with the ZnO standard pattern (PDF#76-0704) [27, 31], demonstrating the successful fabrication of ZIF-8-derived ZnO (further discussion can be found in Fig. S3 in the ESM). SEM and TEM were employed to examine the morphology and microstructure of the ZIF-8-derived ZnO. As shown in Fig. 1(d), the ZnO sample retains the dodecahedral structure. However, compared to the ZIF-8 sample, the surface of ZIF-8-derived ZnO is significantly roughened with porous structure and the average size is reduced to about 500 nm (Fig. S4 in the ESM), which is consistent with the previous report [32]. The unique morphological structure of ZnO provides more active sites and ion transfer routes, improving the interfacial electrochemical reaction kinetics [33, 34]. Figure 1(e) presents a high-resolution TEM image of the ZnO NCs and the lattice spacing is 0.282 nm, corresponding to the (100) plane of the ZnO NCs. Figure 1(f) displays the selected area electron diffraction (SAED) pattern of ZnO NCs. The SAED pattern reveals several diffraction rings corresponding to the (100), (110), (112), (101), and (102) planes of ZnO, which agrees well with the XRD pattern, indicating the polycrystalline nature of the ZnO NCs.

The PEC photoresponse of ZnO NCs was assessed by a three-electrode system, where ZnO NCs photoelectrodes, Pt wire, saturated calomel electrode, and 0.1 M KOH aqueous solution served as working electrode, counter electrode, reference electrode, and electrolyte. When n-type ZnO contacts the electrolyte, an upward band bending forms at the ZnO/electrolyte interface pointing from ZnO to electrolyte due to the establishment of electrochemical equilibrium. Under UV irradiation, photogenerated holes migrate toward the ZnO surface, where they undergo oxidation reactions with hydroxide ions (OH^-) to produce hydroxyl radicals (OH*). Meanwhile, photogenerated electrons flow through the external circuit to the counter electrode. The generated OH* then undergoes a reduction reaction with the photogenerated electrons at the counter electrode, producing a positive photocurrent (Fig. S5 in the ESM) [14]. Figure S6 in the ESM shows the voltage-dependent photoresponse of the ZnO NCs PEC PDs under 365 nm irradiation (level I). The device exhibits weak voltage dependence and good self-powered capability. Both the photoresponse and dark current density slightly increase as the voltage increases, therefore, we focus on self-powered photoresponse in the following. Then, the current density–time (J–t) curves of ZnO NCs PEC photoluminescent devices were attained in self-powered mode under the irradiation of cyclic switching wavelength at 365 nm. As shown in Fig. 2(a), the devices show stable and repeatable UV photoresponse. To quantitatively evaluate the performance of ZnO NCs PEC PDs, the key parameters including J_{ph}, R, and specific detectivity (D^*) are calculated via the following formulas: $J_{ph} = J_i - J_d$ (J_i and J_d represent the current density with and without irradiation), $R = J_{ph}/P$, and $D^* = R \times S^{1/2}/(2q \times J_d \times S)^{1/2}$, respectively, where P represents the light power intensity (see Table S1 in the ESM), S is the effective area of the ZnO NCs (1 cm × 1 cm), and q denotes the electron charge of 1.60×10^{-19} C. Apparently, the J_{ph} increases with the elevated P, and J_{ph} is about 26.75 μA/cm² at level I, which increases to 333.12 μA/cm² at level V (more details in Table S2 in the ESM). The R and D^* of ZnO NCs are as high as 300.6 mA/W and 3.58×10^{11} Jones, as shown in Fig. 2(b), and Tables S3 and S4 in the ESM.

Spectral selectivity is a key parameter for visible-blind UV PDs, representing the ability to anti-interference visible light in complex environments, denoted as the UV–visible rejection ratio ($R_{365\ nm}/R_{405\ nm}$). The UV–visible rejection ratio ($R_{365\ nm}/R_{405\ nm}$) of the ZnO NCs PEC PDs was calculated to be 2000, demonstrating excellent spectral selectivity (Fig. 2(c)). The fast response speed is crucial for practical applications, reflected by rise time (t_{ris}) and

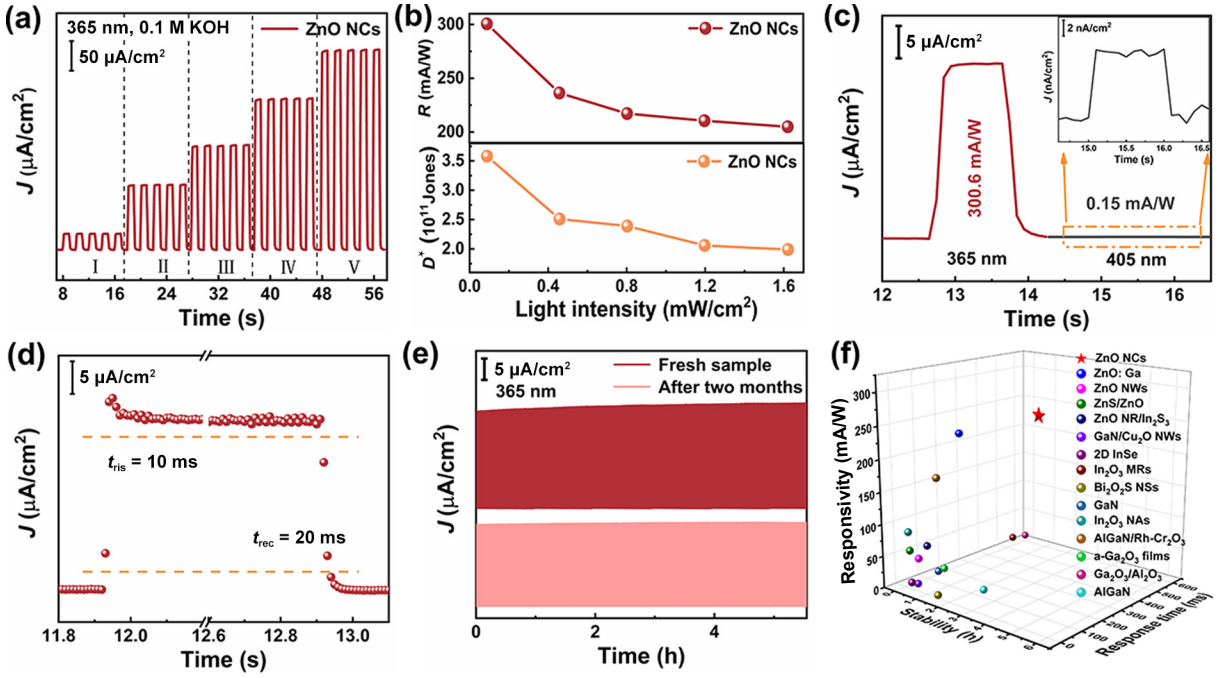

Figure 2 Photoresponse of self-powered ZnO NCs PEC UV PDs. (a) *J*–*t* curves irradiated by 365 nm with different light power intensities. (b) The corresponding *R* and D^* values. (c) *J*–*t* curves of ZnO NCs PEC VBUV PDs irradiated at 365 and 405 nm. Inset: *J*–*t* plot at 405 nm. (d) Intervals between t_{ris} and t_{rec} of ZnO NCs. (e) Cyclic stability test of ZnO NCs at 365 nm for 10,000 cycles (level I). (f) Performance comparison of recently reported self-powered PEC UV PDs. ZnO:Ga [27], ZnO NWs [38], ZnS/ZnO [26], ZnO NR/In_2S_3 [39], GaN/Cu_2O NWs [40], 2D InSe [41], In_2O_3 MRs [14], Bi_2O_2S NSs [42], GaN [43], In_2O_3 Nas [44], AlGaN/Rh-Cr_2O_3 [45], a-Ga_2O_3 films [46], Ga_2O_3/Al_2O_3 [47], and AlGaN [48].

recovery time (t_{rec}). The t_{ris} (t_{rec}) is defined as the time that J_{ph} increases (decreases) from 10% (90%) to 90% (10%). The ZnO NCs exhibit a t_{ris} of 10 ms and t_{rec} of 20 ms, indicating the fast response speed, as shown in Fig. 2(d). Excitingly, ZnO NCs PEC PDs showed excellent stability over 5.56 h (10,000 cycles) with the J_{ph} remaining with almost no attenuation. As shown in Fig. S7 in the ESM, the ZnO NCs are without structural degradation after the 5.56 h multicycle test, further demonstrating excellent stability. We intercepted the multi-cycle *J*–*t* curves at different time intervals to further demonstrate good multi-cycle stability (as shown in Fig. S8 in the ESM). In addition, after two months of storage under drying at room temperature, J_{ph} decreased from 26.19 to 20.42 μA/cm² under 365 nm irradiation (level I), maintaining 78% of the initial value (Fig. 2(e)), indicating good long-term stability. The long-term stability of ZnO NCs photoanodes can be further enhanced by coating the hydrogel protective layer [35]. To further demonstrate the advantages of ZnO NCs, we also explore the UV photoresponse of ZIF-8 derived ZnO NPs, and the photoresponse performance is shown in Fig. S9 in the ESM. The ZnO NPs PEC UV PDs show inferior UV detection capability with a low responsivity (41.35 mA/W), slow response speed (200/300 ms), low spectral selectivity (UV/visible rejection ratio of 100.36), and poor stability (J_{ph} retaining 76% after 500 cycles). Compared with previously reported self-powered PEC UV PDs, our ZnO NCs PEC UV PDs stand out due to ultrahigh UV responsivity, outstanding spectral selectivity, excellent cyclic stability, and fast response speed (Table S5 in the ESM and Fig. 2(f)), making them promising candidates for high-performance UV photodetection applications.

Another effective way to modulate the performance of PEC PDs is by controlling the mass transfer process and interfacial redox reaction kinetics by regulating electrolyte concentration [36]. Therefore, we further investigated the impact of electrolyte concentration on the performance of PEC PDs. Specifically, the J_{ph} is 13.80 μA/cm² in 0.01 M KOH, which increases to 24.33 and 26.19 μA/cm² as the concentration of the KOH solution increases to 0.05 and 0.1 M (Fig. S10(a) in the ESM), indicating the J_{ph} were close to saturation as the KOH solution concentration is larger than 0.05 M. Therefore, higher electrolyte concentrations were not used in our experiment. The electrochemical impedance spectroscopy (EIS) of ZnO NCs PEC UV PDs in varying electrolyte concentrations were measured to illustrate the effect of electrolyte concentration on PEC properties. The EIS results and corresponding equivalent current diagrams are presented in Fig. S10(b) and Table S6 in the ESM. At higher electrolyte concentrations, the devices exhibit smaller equivalent series resistances (R_s) and charge transfer resistances (R_{ct}), indicating improved ionic conductivity and charge transfer kinetics, which result in enhanced UV photoresponse [37]. To further explore the application of ZnO NCs in different aqueous environments, we tested them in 0.1 M Na_2SO_4 and simulated seawater as in Figs. S10(c) and S10(d) in the ESM. The results show that the J_{ph} of ZnO NCs in these two electrolytes are 9.93 (0.1 M Na_2SO_4) and 5.70 μA/cm² (simulated seawater) at level I, demonstrating good UV photoresponse in diversified environments.

To clarify the high-performance UV photoresponse of ZnO NCs, we analyze the light absorption properties, photogenerated carrier separation, and interfacial electrochemical reaction kinetics of both ZnO samples. As shown in Fig. 3(a), ZnO NCs provide superior UV absorption due to the light multiple reflection absorption induced by the NCs structure [49]. The morphology of ZnO NPs is shown in Fig. S11 in the ESM, where they are formed by the stacking of irregular small particles, which results in weakened light absorption. The corresponding optical bandgaps of ZnO NCs and NPs calculated from the Tauc plot are 3.36 and

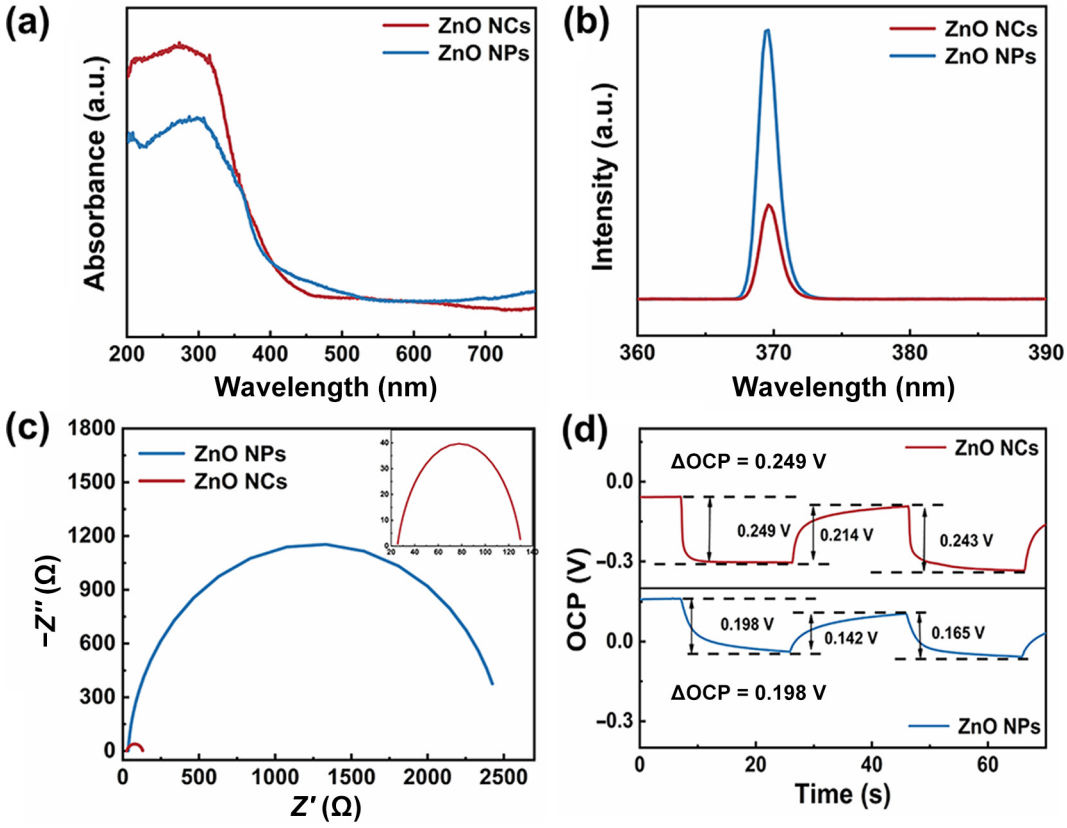

Figure 3 (a) UV–vis diffuse reflectance spectra. (b) Photoluminescence spectra. (c) EIS of ZnO samples. (d) ΔOCP is the difference in voltage between the dark and λ = 365 nm illumination conditions.

3.25 eV (Fig. S12 in the ESM). The slightly decreased optical bandgap of ZnO NPs is due to a little increased oxygen vacancy (V_O) concentration, demonstrated by the XPS and electron paramagnetic resonance (EPR) results (more detail in Fig. S13 in the ESM) [50, 51]. Figure 3(b) displays the PL spectra of both samples, providing insight into the effect of morphology on photogenerated carrier separation. Compared to ZnO NPs, the PL intensity of ZnO NCs is significantly reduced, indicating more efficient photogenerated carrier separation and suppression of photogenerated electron-hole recombination [52, 53].

To thoroughly investigate interfacial electrochemical behavior, we conducted EIS (Fig. 3(c)) and open-circuit potential (OCP) testing (Fig. 3(d)). The R_s and R_{ct} values of ZnO NCs and ZnO NPs are given in Table S7 in the ESM. A smaller R_s can accelerate the transport of charge carriers and reduce the response delay [54, 55]. Therefore, the response speed of ZnO NCs (10 ms) is much faster than that of ZnO NPs (200 ms). The R_{ct} of ZnO NCs and ZnO NPs are 105.3 and 2452.0 Ω, respectively, indicating that the porous NCs can dramatically accelerate the interfacial charge transfer and improve the interfacial electrochemical reaction kinetics. As shown in Fig. S14 in the ESM, the electrochemical active surface area of ZnO NCs (4.0) is estimated to be larger than that of ZnO NPs (1.4) based on the cyclic voltammetry curves, which further suggests that ZnO NCs can provide more electrochemical reaction sites and promote electrochemical reaction kinetics, agreeing well with EIS results. The OCP of ZnO NCs rapidly reaches saturation under irradiation, demonstrating a faster photocarrier separation process. The photovoltage (ΔOCP, $\Delta OCP = OCP_{light} - OCP_{dark}$) of ZnO NCs recovers 86% (0.249/0.214 V) within 10 s after the light is turned off, which is larger than the 72% recovery observed in ZnO NPs (0.198/0.142 V), indicating that the photogenerated carriers in ZnO NCs possess faster relaxation process [53, 54]. The rapid photogenerated carrier transport capability and relaxation process enable ZnO NCs to exhibit fast photoresponse speed. In the second cycle of the test, the OCP_{dark} is mainly determined by the unrelaxed charges, which significantly reduces the photovoltage [13, 56]. In the second cycle, after the light is turned off, the photovoltage of ZnO NCs (0.243 V) is almost equal to that of the initial cycle (0.249 V) and larger than that of ZnO NPs (0.165 V), accelerating the interfacial charge transfer, which agrees well with EIS results.

To further validate the performance of ZnO PEC PDs in underwater optical imaging capability, the device is employed as the single point-like sensing pixel in an imaging system as shown in Fig. 4(a). The system consists of a 365 nm laser source, source meter, oscilloscope, computer, and a hollow board with an "LXH" hollow mark. The object can be precisely moved in both horizontal and vertical directions (x–y plane), with this controlled by the computer system. We also provide a digital image of the underwater optical imaging system in Fig. S15 in the ESM. A 370 × 120 pixel image can be obtained at a bias voltage of −0.5 V as shown in Fig. 4(b). The image demonstrates high fidelity, featuring distinct boundaries and exhibiting a high degree of correspondence with the shape of the target object. Additionally, Fig. 4(c) shows the intensity profile of the blue line region in Fig. 4(b), where the sharp intensity variations (rapid rises and falls) further demonstrate that the system has a high dynamic range, capable of accurately capturing subtle variations in the image. These good imaging results highlight the significant potential of ZnO NCs PEC UV PDs in underwater optical imaging applications, confirming its reliability and effectiveness in high dynamic range imaging.

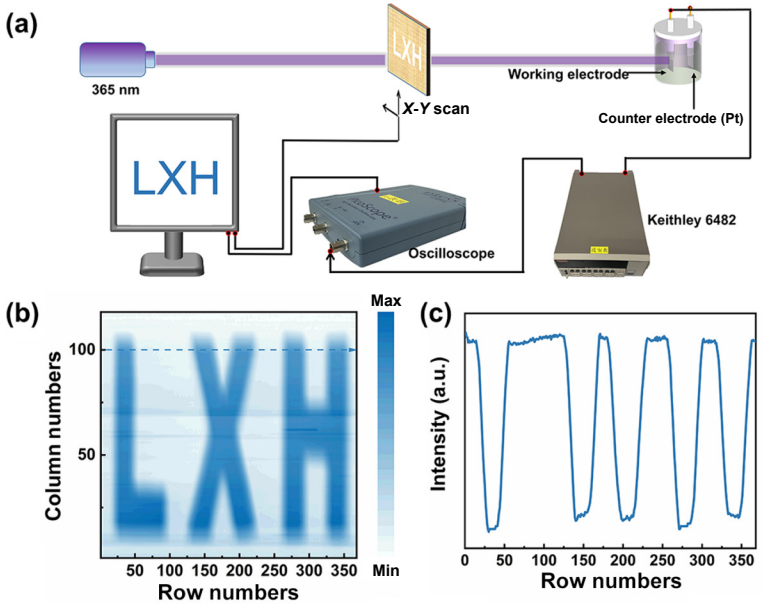

Figure 4 Underwater optical imaging application. (a) Schematic diagram of the underwater optical imaging system. (b) Image obtained from the image scanning system. (c) The profile of the blue line of (b).

4 Conclusions

This work demonstrates that topography engineering is a powerful tool to improve the UV photoresponse of ZnO PEC PDs and proves the high-performance PEC UV PDs based on ZnO NCs. The ZnO NCs-based PEC PDs have achieved high-performance self-powered photoresponse at 365 nm, with a R of up to 300.6 mA/W, a fast response time (10/20 ms), outstanding spectra selectivity, and excellent cycling stability (10,000 cycles). The outstanding UV photoresponse is attributed to the NCs structure, effectively improving UV absorption, promoting photogenerated carrier separation, and accelerating interfacial electrochemical reaction kinetics. Furthermore, the self-powered ZnO-based PEC PDs have good underwater optical imaging capability. This work offers a new insight into designing high-performance underwater UV optoelectronic devices.

Electronic Supplementary Material: Supplementary material (methods and additional characterization results, including Figs. S1–S15 and Tables S1–S7) is available in the online version of this article at https://doi.org/10.26599/NR.2025.94907403.

Data availability

All data needed to support the conclusions in the paper are presented in the manuscript and the Electronic Supplementary Material. Additional data related to this paper may be requested from the corresponding author upon request.

Acknowledgements

The authors gratefully acknowledge support from the Natural Science Foundation of Heilongjiang Province, China (No. PL2024E001).

Declaration of competing interest

The authors declare no conflicts of interest. They have no known competing financial interests or personal relationships that could have appeared to influence the work reported in this paper.

Author contribution statement

X. H. L. and S. Z. T.: Conceptualization, experimental design, data curation, validation, writing manuscript. Y. Z., D. Y. T., X. R. H., W. H. L., J. X. Z., N. N. Z., S. Z., and J. Y.: Data curation, analysis. F. G. and W. F.: Conceptualization, supervision, project administration, funding acquisition, writing – review & editing. All the authors have approved the final manuscript.

Use of AI statement

None.

References

[1] Cao, F.; Liu, Y.; Liu, M.; Han, Z. Y.; Xu, X. B.; Fan, Q. L.; Sun, B. Wide bandgap semiconductors for ultraviolet photodetectors: Approaches, applications, and prospects. *Research* **2024**, *7*, 0385.

[2] Zhang, Y.; Cai, Y.; Zhou, J.; Xie, Y.; Xu, Q. W.; Zou, Y.; Guo, S. S.; Xu, H. X.; Sun, C. L.; Liu, S. Surface acoustic wave-based ultraviolet photodetectors: A review. *Sci. Bull.* **2020**, *65*, 587–600.

[3] Han, P.; Geng, Y. J.; Guo, F. Y.; Gao, S. Y.; Zhang, Y. Alkali metal ion passivation of lead-free perovskite film for high responsivity self-powered broadband photodetectors. *Chem. Eng. J.* **2024**, *490*, 151876.

[4] Li, Z. Q.; Yan, T. T.; Fang, X. S. Low-dimensional wide-bandgap semiconductors for UV photodetectors. *Nat. Rev. Mater.* **2023**, *8*, 587–603.

[5] Wang, K. T.; Wang, H. L.; Chen, C. M.; Li, W. J.; Wang, L.; Hu, F.; Gao, F. M.; Yang, W. Y.; Wang, Z. X.; Chen, S. L. High-performance ultraviolet photodetector based on single-crystal integrated self-supporting 4H-SiC nanohole arrays. *ACS Appl. Mater. Interfaces* **2023**, *15*, 23457–23469.

[6] Ding, K.; Zhang, H.; Jiang, J. L.; Luo, J. S.; Wu, R. L.; Ye, L. J.; Tang, Y.; Pang, D.; Li, H. L.; Li, W. J. Balancing carrier dynamics in oxygen-vacancy-tuned amorphous Ga_2O_3 thin-film self-powered photoelectrochemical-type solar-blind photodetector arrays for underwater imaging. *Adv. Sci.* **2024**, *11*, 2407822.

[7] Wang, H. L.; Li, W. J.; Gloginjić, M.; Petrović, S.; Krupska, T. V.; Turov, V. V.; Zhao, J. L.; Yang, W. Y.; Du, Z. T.; Chen, S. L. High-sensitivity photoelectrochemical ultraviolet photodetector with Stable pH-universal adaptability based on whole single-crystal integrated self-supporting 4H-SiC nanoarrays. *Small* **2024**, *20*, 2400045.

[8] Zhou, S. Q.; Jiang, C. X.; Han, J. L.; Mu, Y. Q.; Gong, J. R.; Zhang, J. High-performance self-powered PEC photodetectors based on 2D $BiVO_4$/MXene Schottky junction. *Adv. Funct. Mater.* **2025**, *35*, 2416922.

[9] Li, L. A.; Fang, S.; Chen, W.; Li, Y. Y.; Vafadar, M. F.; Wang, D. H.; Kang, Y.; Liu, X.; Luo, Y. M.; Liang, K. et al. Facile semiconductor p-n homojunction nanowires with strategic p-Type doping engineering combined with surface reconstruction for biosensing applications. *Nano-Micro Lett.* **2024**, *16*, 192.

[10] Zou, B. C.; Chen, C. M.; Sun, L.; Lin, Y.; Liu, Z. H.; Li, W. J.; Wang, L.; Gao, F. M.; He, H.; Yang, W. Y. et al. Self-powered high-responsivity self-supporting SiC/SnO_2 nanoarray photoelectrochemical ultraviolet photodetector: Toward all-scenario harsh underwater applications. *Adv. Funct. Mater.* **2024**, 202421819.

[11] Zi, Y.; Hu, Y.; Pu, J. M.; Wang, M. K.; Huang, W. C. Recent progress in interface engineering of nanostructures for photoelectrochemical energy harvesting applications. *Small* **2023**, *19*, 2208274.

[12] Lu, C. H.; Dong, W.; Zou, Y. Q.; Wang, Z. Y.; Tan, J. Y.; Bai, X.; Ma, N.; Ge, Y. Q.; Zhao, Q. Y.; Xu, X. L. Direct Z-scheme $SnSe_2$/SnSe heterostructure passivated by Al_2O_3 for highly stable and sensitive photoelectrochemical photodetectors. *ACS Appl. Mater. Interfaces* **2023**, *15*, 6156–6168.

[13] Lu, C. H.; Luo, M. W.; Dong, W.; Ge, Y. Q.; Han, T. T.; Liu, Y. Q.; Xue, X. Y.; Ma, N.; Huang, Y. Y.; Zhou, Y. X. et al. Bi_2Te_3/Bi_2Se_3/Bi_2S_3 cascade heterostructure for fast-response and high-photoresponsivity photodetector and high-efficiency water splitting with a small bias voltage. *Adv. Sci.* **2022**, *10*, 2205460.

[14] Cui, M. Q.; Shao, Z. T.; Qu, L. H.; Liu, X.; Yu, H.; Wang, Y. X.; Zhang, Y. X.; Fu, Z. D.; Huang, Y. W.; Feng, W. MOF-derived In_2O_3 microrods for high-performance photoelectrochemical ultraviolet photodetectors. *ACS Appl. Mater. Interfaces* **2022**, *14*, 39046–39052.

[15] Yu, H.; Shao, Z. T.; Wang, Y. X.; Xu, Y.; Zhang, X. Y.; Yao, J.; Gao, F.; Hu, P. A.; Feng, W. One stone, three birds: SnO_2 nanosheet arrays toward self-powered visible-blind UV photodetection with high responsivity and rejection ratio. *Adv. Opt. Mater.* **2024**, *12*, 2301460.

[16] Zou, B. C.; Yang, Y.; Wang, H. L.; Li, W. J.; Wang, L.; Gao, F. M.; Zhang, D. D.; Gloginjić, M.; Erić, M.; Petrović, S. et al. High-responsivity self-powered photoelectrochemical UV photodetector based on integrated self-supporting SiC/ZnS heterojunction nanowire arrays. *Small* **2025**, *21*, 2406308.

[17] Chen, K.; Wang, S. L.; He, C. R.; Zhu, H. W.; Zhao, H. L.; Guo, D. Y.; Chen, Z. W.; Shen, J. Q.; Li, P. G.; Liu, A. et al. Photoelectrochemical self-powered solar-blind photodetectors based on Ga_2O_3 nanorod array/electrolyte solid/liquid heterojunctions with a large separation interface of photogenerated carriers. *ACS Appl. Nano Mater.* **2019**, *2*, 6169–6177.

[18] Li, X. D.; Gao, C. T.; Duan, H. G.; Lu, B. G.; Pan, X. J.; Xie, E. Q. Nanocrystalline TiO_2 film based photoelectrochemical cell as self-powered UV-photodetector. *Nano Energy* **2012**, *1*, 640–645.

[19] Zhou, X.; Ye, L. J.; Yuan, L.; Zhang, D.; Zhang, H.; Pang, D.; Tang, Y.; Li, H. L.; Li, W. J.; Zeng, H. P. Mg-doped α-Ga_2O_3 nanorods for the construction of photoelectrochemical-type self-powered solar blind UV photodetectors and underwater imaging application. *Adv. Sci.* **2025**, 2413074.

[20] Wang, L.; Palacios-Padrós, A.; Kirchgeorg, R.; Tighineanu, A.; Schmuki, P. Enhanced photoelectrochemical water splitting efficiency of a hematite-ordered Sb: SnO_2 host-guest system. *ChemSusChem* **2014**, *7*, 421–424.

[21] Xu, F. Y.; Yan, W. J.; Pang, D.; Ren, B. N.; Tang, Q. X.; Wang, X.; Tan, G. Y.; Li, H. L.; Xiong, Y. Q.; Tang, Y. et al. High-performance photoelectrochemical (PEC) type self-powered ultraviolet photodetectors (PDs) based on three-dimensional ZnO film/carbon fiber paper. *Opt. Mater.* **2024**, *150*, 115185.

[22] Karagoz, E.; Altaf, C. T.; Yesilbag, F. N. T.; Yesilbag, Y. O.; Erdem, E.; Misirlioglu, F. B.; Sankir, N. D.; Sankir, M. Self-powered quasi-solid-state photoelectrochemical photodetectors based on MXene paper modified by ZnO nanostructured architecture. *ACS Appl. Nano Mater.* **2024**, *7*, 7709–7719.

[23] Kazmi, J.; Abbas, A.; Young, D. J.; Shah, J. H.; Ahmad, W.; Shah, S. S. A.; Raza, S. R. A.; Mohamed, M. A.; Govorov, A. O.; Wang, Z. M. ZnO nanowire UV photodetectors: At the intersection of flexibility, biocompatibility, and visible blindness. *Mater. Today* **2024**, *82*, 139–180.

[24] Ouyang, W. X.; Chen, J. X.; Shi, Z. F.; Fang, X. S. Self-powered UV photodetectors based on ZnO nanomaterials. *Appl. Phys. Rev.* **2021**, *8*, 031315.

[25] Li, Q. H.; Wei, L.; Xie, Y. R.; Zhang, K.; Liu, L.; Zhu, D. P.; Jiao, J.; Chen, Y. X.; Yan, S. S.; Liu, G. L. et al. ZnO nanoneedle/H_2O solid–liquid heterojunction-based self-powered ultraviolet detector. *Nanoscale Res. Lett.* **2013**, *8*, 415.

[26] Lin, H. L.; Wei, L.; Wu, C. C.; Chen, Y. X.; Yan, S. S.; Mei, L. M.; Jiao, J. High-performance self-powered photodetectors based on ZnO/ZnS core-shell nanorod arrays. *Nanoscale Res. Lett.* **2016**, *11*, 420.

[27] Tang, Q. X.; Tan, G. Y.; Zhang, H.; Li, H. L.; Xiong, Y. Q.; Pang, D.; Ye, L. J.; Fang, L.; Kong, C. Y.; Li, W. J. Enhanced photoresponse of self-powered ZnO-based photoelectrochemical-type UV photodetectors via Ga-doping for optical communication application. *J. Alloy. Compd.* **2024**, *972*, 172864.

[28] Morris, W.; Stevens, C. J.; Taylor, R. E.; Dybowski, C.; Yaghi, O. M.; Garcia-Garibay, M. A. NMR and X-ray study revealing the rigidity of zeolitic imidazolate frameworks. *J. Phys. Chem. C* **2012**, *116*, 13307–13312.

[29] Jiang, M.; Zhang, J. Y.; Yang, W. X.; Wu, D. M.; Zhao, Y. K.; Wu, Y. Y.; Zhou, M.; Lu, S. L. Flexible self-powered photoelectrochemical photodetector with ultrahigh detectivity, ultraviolet/visible reject ratio, stability, and a quasi-invisible functionality based on lift-off vertical (Al, Ga)N nanowires. *Adv. Mater. Interfaces* **2022**, *9*, 2200028.

[30] Ning, Y.; Zhang, Z. M.; Teng, F.; Fang, X. S. Novel transparent and self-powered UV photodetector based on crossed ZnO nanofiber array homojunction. *Small* **2018**, *14*, 1703754.

[31] Deka Boruah, B.; Misra, A. Energy-efficient hydrogenated zinc oxide nanoflakes for high-performance self-powered ultraviolet photodetector. *ACS Appl. Mater. Interfaces* **2016**, *8*, 18182–18188.

[32] Pan, L.; Muhammad, T.; Ma, L.; Huang, Z. F.; Wang, S. B.; Wang, L.; Zou, J. J.; Zhang, X. W. MOF-derived C-doped ZnO prepared via a two-step calcination for efficient photocatalysis. *Appl. Catal. B Environ.* **2016**, *189*, 181–191.

[33] Li, Z. X.; Wu, C. L.; Mao, L. R.; Yin, C. J. Residual-carbon-supported δ-MnO_2 as cathodes for aqueous zinc ion batteries with high specific capacity. *J. Energy Storage* **2025**, *105*, 114760.

[34] Liu, Q.; Fan, G. L.; Zeng, Y. X.; Zhang, X. T.; Luan, D. Y.; Guo, Y.; Gu, X. J.; Lou, X. W. Hollow octahedral Pr_6O_{11}-Mn_2O_3 heterostructures for high-performance aqueous Zn-ion batteries. *Adv. Energy Mater.* **2024**, *14*, 2402743.

[35] Tan, J.; Kang, B.; Kim, K.; Kang, D.; Lee, H.; Ma, S.; Jang, G.; Lee, H.; Moon, J. Hydrogel protection strategy to stabilize water-splitting photoelectrodes. *Nat. Energy* **2022**, *7*, 537–547.

[36] Xue, R. Y.; Shao, Z. T.; Yang, X. X.; Zhang, Y. X.; Fu, Z. D.; Huang, Y. W.; Feng, W. Self-powered photoelectrochemical photodetectors based on electrochemically exfoliated In_2Se_3 nanosheets. *ACS Appl. Nano Mater.* **2022**, *5*, 7036–7041.

[37] Zhang, Y.; Shao, Z. T.; Zhou, J. X.; Sun, S. M.; Sun, R. Y.; Zhang, N. N.; Liu, J. M.; Gao, X. Y.; Hu, P. A.; Feng, W. Vacancy engineering optimizing solid/liquid Interfacial properties for boosting self-powered solar-blind photodetection. *Adv. Opt. Mater.* **2024**, *12*, 2401639.

[38] Ji, Y.; Wu, L. Y.; Liu, Y.; Yang, Y. Chemo-phototronic effect induced electricity for enhanced self-powered photodetector system based on ZnO nanowires. *Nano Energy* **2021**, *89*, 106449.
[39] Eroglu, A. N.; Altaf, C. T.; Sankir, N. D.; Sankir, M. Patterned ZnO nanorods/indium sulfide based self-powered photoelectrochemical photodetectors. *Opt. Mater.* **2024**, *148*, 114763.
[40] Luo, M. R.; Song, J. X.; Wang, J. L.; Pan, X. C.; Hong, H.; Nötzel, R. Ultraviolet photoelectrochemical photodetector based on GaN/Cu_2O core–shell nanowire p-n heterojunctions. *AIP Adv.* **2022**, *12*, 115112.
[41] Yang, X. X.; Liu, X.; Qu, L. H.; Gao, F.; Xu, Y.; Cui, M. Q.; Yu, H.; Wang, Y. X.; Hu, P. G.; Feng, W. Boosting photoresponse of self-powered InSe-based photoelectrochemical photodetectors via suppression of interface doping. *ACS Nano* **2022**, *16*, 8440–8448.
[42] Yang, X. X.; Qu, L. H.; Gao, F.; Hu, Y. X.; Yu, H.; Wang, Y. X.; Cui, M. Q.; Zhang, Y. X.; Fu, Z. D.; Huang, Y. W. et al. High-performance broadband photoelectrochemical photodetectors based on ultrathin Bi_2O_2S nanosheets. *ACS Appl. Mater. Interfaces* **2022**, *14*, 7175–7183.
[43] Chen, K.; Zhang, D. Q.; Shao, P. F.; Zhi, T.; Zhao, J. G.; Sang, Y. M.; Hu, W. X.; Ye, Y. C.; Xue, J. J.; Chen, D. J. et al. Ordered GaN nanorod arrays for self-powered photoelectrochemical ultraviolet photodetectors. *ACS Appl. Nano Mater.* **2022**, *5*, 13149–13157.
[44] Zhang, N. N.; Gao, X. Y.; Guan, H. R.; Sun, S. M.; Liu, J. M.; Shao, Z. T.; Gao, Q. Y.; Zhang, Y.; Sun, R. Y.; Yang, G. et al. Three-dimensional porous In_2O_3 arrays for self-powered transparent solar-blind photodetectors with high responsivity and excellent spectral selectivity. *Nano Res.* **2024**, *17*, 4471–4477.
[45] Liu, X.; Wang, D. H.; Shao, P. F.; Sun, H. D.; Fang, S.; Kang, Y.; Liang, K.; Jia, H. F.; Luo, Y. M.; Xue, J. J. et al. Achieving record high external quantum efficiency > 86.7% in solar-blind photoelectrochemical photodetection. *Adv. Funct. Mater.* **2022**, *32*, 2201604.
[46] Huang, L. J.; Hu, Z. R.; Zhang, H.; Xiong, Y. Q.; Fan, S. Q.; Kong, C. Y.; Li, W. J.; Ye, L. J.; Li, H. L. A simple, repeatable and highly stable self-powered solar-blind photoelectrochemical-type photodetector using amorphous Ga_2O_3 films grown on 3D carbon fiber paper. *J. Mater. Chem. C* **2021**, *9*, 10354–10360.
[47] Zhang, J. H.; Jiao, S. J.; Wang, D. B.; Gao, S. Y.; Wang, J. Z.; Zhao, L. C. Nano tree-like branched structure with α-Ga_2O_3 covered by γ-Al_2O_3 for highly efficient detection of solar-blind ultraviolet light using self-powered photoelectrochemical method. *Appl. Surf. Sci.* **2021**, *541*, 148380.
[48] Wang, D. H.; Liu, X.; Fang, S.; Huang, C.; Kang, Y.; Yu, H. B.; Liu, Z. L.; Zhang, H. C.; Long, R.; Xiong, Y. J. et al. Pt/AlGaN nanoarchitecture: Toward high responsivity, self-powered ultraviolet-sensitive photodetection. *Nano Lett.* **2020**, *21*, 120–129.
[49] Wang, W. H.; Qi, L. M. Light management with patterned micro- and nanostructure arrays for photocatalysis, photovoltaics, and optoelectronic and optical devices. *Adv. Funct. Mater.* **2019**, *29*, 1807275.
[50] Li, J.; Tang, X. G.; Liu, Q. X.; Jiang, Y. P.; Tang, Z. X. Resistive switching and optical properties of strontium ferrate titanate thin film prepared via chemical solution deposition. *J. Adv. Ceram.* **2021**, *10*, 1001–1010.
[51] Siddique, F.; Nasir, A.; Syrek, K.; Sulka, G. D.; Gonzalez-Cortes, S.; Li, C. B.; Zhang, X. M.; Wierzbicka, E. Novel synthesis of reduced PdO-WO_3 hybrids for enhanced photoelectrochemical water splitting. *J. Alloy. Compd.* **2025**, *1010*, 177615.
[52] Abd-Elrahim, A. G.; Chun, D. M. Facile one-step deposition of ZnO-graphene nanosheets hybrid photoanodes for enhanced photoelectrochemical water splitting. *J. Alloy. Compd.* **2021**, *870*, 159430.
[53] Fang, S.; Li, L. A.; Wang, D. H.; Chen, W.; Kang, Y.; Wang, W. Y.; Liu, X.; Luo, Y. M.; Yu, H. B.; Zhang, H. C. et al. Breaking the responsivity-bandwidth trade-off limit in GaN photoelectrodes for high-response and fast-speed optical communication application. *Adv. Funct. Mater.* **2023**, *33*, 2214408.
[54] Yang, T.; Chen, Z. W.; Yue, X. Z.; Liu, Q. C.; Yi, S. S.; Zhu, Y. F. Interfacial charge transfer bridge prolongs carrier recombination lifetimes of CoFe metal-thiolate framework/hematite photoanode for water oxidation. *Adv. Funct. Mater.* **2024**, *34*, 2313767.
[55] Ma, N.; Liu, J. H.; Shao, P. P.; Jia, L.; Lu, C. H.; Zhou, Y. X.; Xu, X. L. Self-surface-oxidation protection of type-I Te/SnS_2 heterostructure based photodetectors for high-stability and fast-speed underwater optical communication application. *Chem. Eng. J.* **2025**, *505*, 159413.
[56] Kamimura, J.; Bogdanoff, P.; Ramsteiner, M.; Corfdir, P.; Feix, F.; Geelhaar, L.; Riechert, H. p-type doping of GaN nanowires characterized by photoelectrochemical measurements. *Nano Lett.* **2017**, *17*, 1529–1537.